Chemical Science

ROYAL SOCIETY OF CHEMISTRY

EDGE ARTICLE

View Article Online
View Journal | View Issue

Cite this: *Chem. Sci.*, 2020, **11**, 7379

All publication charges for this article have been paid for by the Royal Society of Chemistry

Heterometallic multinuclear nodes directing MOF electronic behavior†

Otega A. Ejegbavwo,‡[a] Anna A. Berseneva, ‡[a] Corey R. Martin,[a] Gabrielle A. Leith, [a] Shubham Pandey,[d] Amy J. Brandt,[a] Kyoung Chul Park,[a] Abhijai Mathur,[a] Sharfa Farzandh,[a] Vladislav V. Klepov, [a] Brittany J. Heiser,[a] Mvs Chandrashekhar, [b] Stavros G. Karakalos, [c] Mark D. Smith, [a] Simon R. Phillpot, [d] Sophya Garashchuk, [a] Donna A. Chen *[a] and Natalia B. Shustova *[a]

Metal node engineering in combination with modularity, topological diversity, and porosity of metal–organic frameworks (MOFs) could advance energy and optoelectronic sectors. In this study, we focus on MOFs with multinuclear heterometallic nodes for establishing metal–property trends, *i.e.*, connecting atomic scale changes with macroscopic material properties by utilization of inductively coupled plasma mass spectrometry, conductivity measurements, X-ray photoelectron and diffuse reflectance spectroscopies, and density functional theory calculations. The results of Bader charge analysis and studies employing the Voronoi–Dirichlet partition of crystal structures are also presented. As an example of frameworks with different nodal arrangements, we have chosen MOFs with mononuclear, binuclear, and pentanuclear nodes, primarily consisting of first-row transition metals, that are incorporated in HHTP-, BTC-, and NIP-systems, respectively ($HHTP^{3-}$ = triphenylene-2,3,6,7,10,11-hexaone; BTC^{3-} = 1,3,5-benzenetricarboxylate; and NIP^{2-} = 5-nitroisophthalate). Through probing framework electronic profiles, we demonstrate structure–property relationships, and also highlight the necessity for both comprehensive analysis of trends in metal properties, and novel avenues for preparation of heterometallic multinuclear isoreticular structures, which are critical components for on-demand tailoring of properties in heterometallic systems.

Received 31st May 2020
Accepted 25th June 2020

DOI: 10.1039/d0sc03053h

rsc.li/chemical-science

Introduction

Engineering modular integrative metal platforms, primarily applied in optoelectronic and energy sectors, could bridge the gap between current technology and the great demands for evolving industrial needs.[1–14] Metal–organic frameworks (MOFs) provide a unique opportunity for tailoring material properties of interest through metal node engineering.[15–22] In particular, the framework topology, ensemble size of the secondary building block, nature of the metal, and presence of unsaturated metal sites can be used as variables for property tunability. Integration of a second metal provides an additional degree of freedom for manipulating or fine-tuning the material

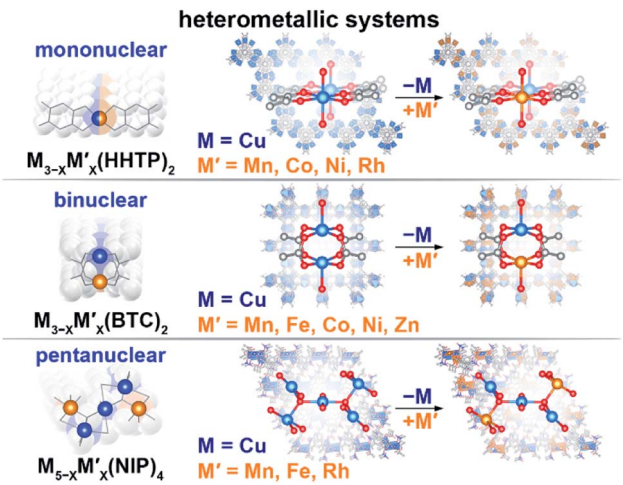

Scheme 1 Schematic representation of the studied heterometallic MOFs: (top) mononuclear $M_{3-x}M'_x(HHTP)_2$, (middle) binuclear $M_{3-x}M'_x(BTC)_2$, and (bottom) pentanuclear $M_{5-x}M'_x(NIP)_4$ systems.

[a]*Department of Chemistry and Biochemistry, University of South Carolina, Columbia, South Carolina 29208, USA. E-mail: shustova@sc.edu*

[b]*Department of Electrical Engineering, University of South Carolina, Columbia, South Carolina 29208, USA*

[c]*College of Engineering and Computing, University of South Carolina, Columbia, South Carolina 29208, USA*

[d]*Department of Materials Science and Engineering, University of Florida, Gainesville, Florida 32611, USA*

† Electronic supplementary information (ESI) available. CCDC 2001459–2001464. For ESI and crystallographic data in CIF or other electronic format see DOI: 10.1039/d0sc03053h

‡ These authors contributed equally.

profile through variation of the metal-to-metal ratio or charge re-distribution.[23–27]

Herein, we utilize the versatility of metal node nuclearity to establish possible metal–property trends for frameworks containing mononuclear, binuclear, and pentanuclear heterometallic nodes (Scheme 1). We demonstrate changes in the electronic profile as a function of integration of a second metal. Furthermore, we probe changes in the electronic structure as a function of metal ensemble size (*i.e.*, number of metal ions in the metal node), metal nature, and metal ratio (in the example of three series). With support from theoretical modeling, we demonstrate that the experimentally studied changes in the density of states (DOS) near the Fermi edge, distribution of the charge on the metal, as well as band gap and conductivity values correlate with each other and are governed by the nature of the second integrated metal.

Results and discussion

We have chosen frameworks with distinct nuclearity that can accommodate different pairs of metals in their scaffolds. Thus, we studied $M_{3-X}M'_X(HHTP)_2$ (M′ = Mn, Co, Ni, and Rh, M = Cu; $HHTP^{3-}$ = triphenylene-2,3,6,7,10,11-hexaone, Fig. 1 and S1†) containing mononuclear metal nodes, $M_{3-X}M'_X(BTC)_2$ (M′ = Mn, Fe, Co, Ni, and Zn, M = Cu; BTC^{3-} = 1,3,5-benzenetricarboxylate, Fig. 1, 2, and S1†) with two metal sites per secondary building unit (SBU; binuclear metal nodes), and $M_{5-X}M'_X(NIP)_4$ (M′ = Mn, Fe, and Rh, M = Cu; NIP^{2-} = 5-nitroisophthalate; Fig. 1, and S1†) with pentanuclear metal nodes.

Comprehensive MOF analysis was performed using single-crystal X-ray diffraction, powder X-ray diffraction (PXRD), X-ray photoelectron spectroscopy (XPS), inductively coupled plasma mass spectrometry (ICP-MS), conductivity measurements, diffuse reflectance (DR) spectroscopy, thermogravimetric analysis (TGA), and density functional theory (DFT) studies. All prepared heterometallic MOFs were analyzed by PXRD to ensure crystallinity before and after transmetallation. The metal ratio was verified by ICP-MS analysis. Notably, all ICP-MS studies were performed on samples that underwent an extensive washing (∼one week) procedure using a Soxhlet apparatus to remove any residual M′-salts utilized for the integration of a second metal (M′). The discussion in this paper will be organized in the following order: preparation and characterization of the monometallic and corresponding heterometallic frameworks, then comprehensive analysis based on XPS, DR spectroscopy, and conductivity measurements with the support of theoretical modeling. The main emphasis of the presented studies is to reveal possible relationships between the observed experimental and theoretical values as a function of the chosen metal M′, *i.e.*, establishing M′–property trends.

Preparation of monometallic and heterometallic systems

mononuclear heterometallic $M_{3-X}M'_X(HHTP)_2$ frameworks

We used monometallic M–MOFs as a template for integration of the second metal through post-synthetic ion metathesis. For preparation of heterometallic mononuclear $Cu_{2.5}Co_{0.5}$-HHTP, the monometallic parent scaffold, $Co_9(HHTP)_4$, was used; $Cu_3(HHTP)_2$ was used as a precursor for the synthesis of $Cu_{2.0}Mn_{1.0}$-HHTP, $Cu_{1.5}Ni_{1.5}$-HHTP, and $Cu_{2.6}Rh_{0.4}$-HHTP MOFs (Table 1, for more details see ESI†). The choice of the scaffold precursor was determined by feasibility of transmetallation (see more details below), preservation of framework integrity, and reasonable times for cation exchange. The selected experimental conditions are provided in Table 1. The M-HHTP frameworks with **bnn** topology (Fig. 1) consist of two-dimensional layers with alternation that can be changed as a function of the metal.[28] $Cu_3(HHTP)_2$ possesses AAAA stacking while layers in the cobalt-containing $Co_9(HHTP)_4$ structure alternates in the ABAB sequence.[28] These distinct structural changes can be detected by the use of PXRD after the transmetallation procedure. For instance, the PXRD pattern of $Co_9(HHTP)_4$ shows prominent peaks at $2\theta = 4.5°$, 9.2°, and 13.9°

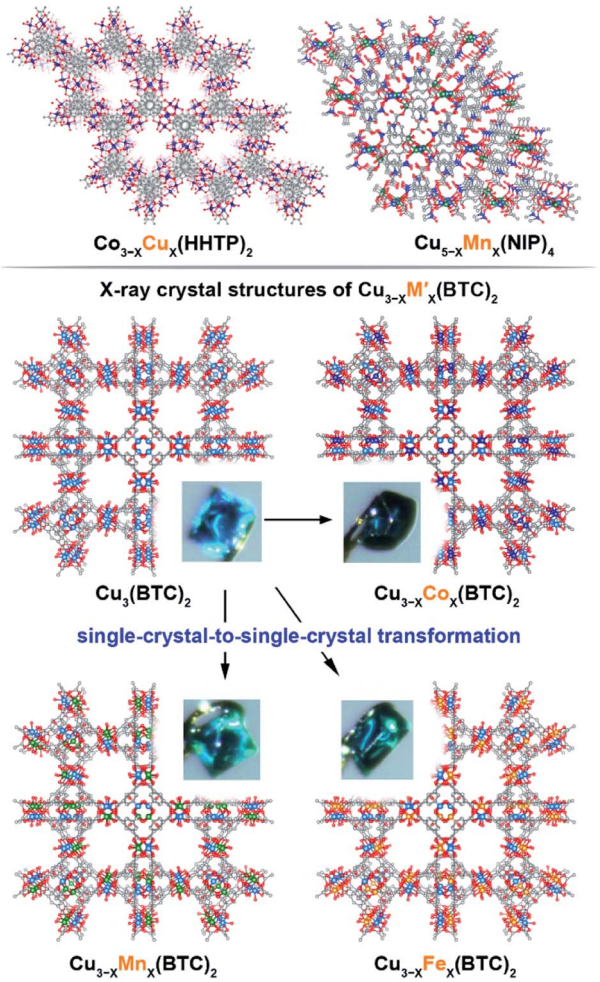

Fig. 1 (Top) Crystal structures of: (left) mononuclear heterometallic $Cu_{3-X}Co_X(HHTP)_2$ [28] and (right) pentanuclear heterometallic $Cu_{5-X}Mn_X(NIP)_4$ MOFs.[29] (bottom) Crystal structures of binuclear monometallic $Cu_3(BTC)_2$ and binuclear heterometallic $Cu_{3-X}M_X$-$(BTC)_2$ (M = Mn, Fe, and Co) MOFs. Insets show photographs of the MOF single crystals. The light blue, dark blue, green, orange, grey, and red spheres represent Cu, Co, Mn, Fe, C, and O atoms, respectively. H atoms were omitted for clarity.

(corresponding to the (100), (200), and (300) reflections, respectively) indicating the long-range order within the *ab* plane (Fig. S2†).[28,30] In the case of $Cu_3(HHTP)_2$, the peak at $2\theta = 13.9°$ (characteristic of $Co_9(HHTP)_4$) is absent in the PXRD pattern while the peak at 12.4° (characteristic of $Cu_3(HHTP)_2$) is detectable (Fig. S2†). In the case of heterometallic $Cu_{3-x}Co_x$(-HHTP)$_2$ MOF, the peak at $2\theta = 13.9°$ in the PXRD pattern (indicative of the presence of the monometallic cobalt-containing MOF) was absent, and the novel peaks at $2\theta =$ 12.4° and 16.4°, characteristic of the monometallic copper-based analogue, are observed (Fig. S2†). These distinct differences in PXRD patterns are in line with the ICP-MS data that demonstrates integration of 83% of copper in the parent Co_9(-HHTP)$_4$ matrix. All MOF samples were analyzed by PXRD to ensure crystallinity before and after transmetallation (Fig. S2 and S3†). PXRD analysis demonstrated that all samples possess AAAA stacking. Thermostability of the $Cu_{3-x}Co_x(HHTP)_2$ samples was studied by TGA and the corresponding TGA plots are shown in Fig. S4.†

Binuclear heterometallic $M_{3-x}M'_x(BTC)_2$ frameworks

The $Cu_3(BTC)_2$ framework, possessing **tbo** topology and containing a binuclear paddle-wheel SBU[31] (Scheme 1, Fig. 1, 3a, and S6†), was used as a template for the synthesis of heterometallic MOFs containing Cu/Fe, Cu/Mn, Cu/Ni, and Cu/Co pairs of metals. As a result, the following compositions were prepared: Cu_mFe_n-BTC, ($m = 2.7$, $n = 0.3$; $m = 2.6$, $n = 0.4$; $m = 2.2$, $n = 0.8$), Cu_mMn_n-BTC, ($m = 2.8$, $n = 0.2$; $m = 2.6$, $n = 0.4$; $m = 2.4$, $n = 0.6$), Cu_mCo_n-BTC, ($m = 2.9$, $n = 0.1$; $m = 2.82$, $n = 0.18$; $m = 2.79$, $n = 0.21$), and Cu_mNi_n-BTC ($m = 2.7$, $n = 0.3$).

Despite the fact that a typical MOF transmetallation procedure results in polycrystalline samples, we were able to preserve single crystals of BTC-based frameworks containing Cu/Fe, Cu/Mn, and Cu/Co pairs. The crystal structures and crystallographic data for the heterometallic $Cu_{2.4}Fe_{0.6}$-BTC, $Cu_{1.8}Fe_{1.2}$-BTC, $Cu_{2.4}Mn_{0.6}$-BTC, $Cu_{2.3}Mn_{0.7}$-BTC, $Cu_{1.9}Co_{1.1}$-BTC, and $Cu_{1.1}Co_{1.9}$-BTC MOFs are shown in Fig. 1 and Tables S1 and S2,† highlighting the isoreticular nature of the monometallic and heterometallic analogues. For the synthesis of the zinc-containing $Cu_{3-x}Zn_x(BTC)_2$ system, a different parent scaffold, $Zn_3(BTC)_2$, was chosen due to unsuccessful attempts to integrate zinc in the copper-containing monometallic framework, $Cu_3(BTC)_2$. Thus, to prepare Cu_mZn_n-BTC, ($m = 1.6$, $n = 1.4$), we soaked $Zn_3(BTC)_2$ in a 1.01 M ethanol solution of $Cu(NO_3)_2$ at room temperature for 24 hours (Table 1). All BTC-based samples were analyzed by PXRD to ensure crystallinity before and after transmetallation (Fig. S7–S12†). Thermostability of the $Cu_{3-x}M'_x(BTC)_2$ samples was determined by TGA and the corresponding TGA plots are shown in Fig. S13–S15.†

Pentanuclear heterometallic $M_{5-x}M'_x(NIP)_4$ frameworks

The $Cu_5(NIP)_4(OH)_2$ ($Cu_5(NIP)_4$)[29] framework was used as a precursor for the synthesis of the corresponding heterometallic $M_{5-x}M'_x(NIP)_4$ systems under the conditions shown in Table 1. In particular, heterometallic MOFs, $Cu_{5-x}M'_x(NIP)_4$ (M′ = Mn, Fe, and Rh), were prepared by soaking or heating

Table 1 Synthesis and evacuation procedures for heterometallic MOFs

Heterometallic MOF	Synthesis T (°C)/time (h)	Evacuation T (°C)/time (h)
$Cu_{2.0}Mn_{1.0}$-HHTP	85/16	85/6
$Cu_{2.5}Co_{0.5}$-HHTP	85/16	85/6
$Cu_{1.5}Ni_{1.5}$-HHTP	85/16	85/6
$Cu_{2.6}Rh_{0.4}$-HHTP	85/16	85/6
$Cu_{2.8}Mn_{0.2}$-BTC	90/24	160/24
$Cu_{2.6}Mn_{0.4}$-BTC	90/48	160/24
$Cu_{2.4}Mn_{0.6}$-BTC	90/72	160/24
$Cu_{2.7}Fe_{0.3}$-BTC	90/24	160/24
$Cu_{2.6}Fe_{0.4}$-BTC	90/48	160/24
$Cu_{2.2}Fe_{0.8}$-BTC	90/72	160/24
$Cu_{2.9}Co_{0.1}$-BTC	90/12	160/24
$Cu_{2.82}Co_{0.18}$-BTC	90/42	160/24
$Cu_{2.79}Co_{0.21}$-BTC	90/72	160/24
$Cu_{2.7}Ni_{0.3}$-BTC	90/74	160/24
$Cu_{1.6}Zn_{1.4}$-BTC	25/24	160/24
$Cu_{4.8}Mn_{0.2}$-NIP	25/3.5	85/12
$Cu_{4.4}Fe_{0.6}$-NIP	25/1	85/12
$Cu_{4.8}Rh_{0.2}$-NIP	60/5	85/12

$Cu_5(NIP)_4$ in an *N*,*N*-dimethylformamide solution of the corresponding chloride M′-salts (more details described in the ESI). Transmetallation resulted in the preparation of novel $Cu_{4.8}Mn_{0.2}$-NIP, $Cu_{4.4}Fe_{0.6}$-NIP, and $Cu_{4.8}Rh_{0.2}$-NIP systems according to ICP-MS analysis. Rapid incorporation of 12% of iron cation inside the $Cu_5(NIP)_4$ lattice occurred even during one hour at room temperature. However, exceeding one hour of transmetallation resulted in loss of framework integrity. A similar crystallinity loss was observed for manganese cation integration after three and a half hours at room temperature. In the case of rhodium transmetallation, $Cu_5(NIP)_4$ preserves its integrity after a five-hour soaking procedure with stirring and heating at a moderate temperature (Table 1). All MOF samples were analyzed by PXRD to ensure crystallinity before and after transmetallation (Fig. S17 and S18†). Thermostability of the $Cu_{5-x}M'_x(NIP)_4$ samples was determined by TGA and the corresponding TGA plots are shown in Fig. S19 and S20.†

Evaluation of M···M Interactions by the Voronoi–Dirichlet Approach. Valence Band Structure, Density of States, Conductivity Measurements, Metal Oxidation States, and Optical Data Analysis in Combination with Theoretical Modeling.

To probe metal···metal interactions in the discussed mononuclear, binuclear, and pentanuclear systems, we employed the Voronoi–Dirichlet tessellation approach.[32,33] In general, a Voronoi–Dirichlet polyhedron (VDP) for a selected atom in the crystal structure is shaped by an intersection of the planes dissecting the center of the lines that connect the selected atom with all surrounding atoms in the structure and are perpendicular to these lines. As a result, every inner point of a VDP is closer to the selected atom than to any other atom in the structure. This approach allows for estimation of interaction strength between two atoms, for instance, metals in the nodes, by calculating the solid angle (Ω) of a shared face of their VDP, expressed as percent of total VDP surface area as shown in eqn (1).[32]

$$\Omega = S/S_{\text{total}} \times 100\% \quad (1)$$

where Ω = solid angle, S = surface area of a face shared between two VDPs, and S_{total} = total surface area of the VDP (Scheme 2).

For performance of the VDP analysis, we need to have access to single-crystal X-ray data, and thus, we chose $Co_9(HHTP)_4$ as an example of the mononuclear system.[28] In $Co_9(HHTP)_4$, the cobalt atoms do not share a common VDP face, indicating no interactions between the metal atoms that is also supported by the distance between the metal atoms of 4.96 Å (Scheme 2). In $Cu_3(BTC)_2$ with binuclear nodes, the shortest distance between the metal atoms is 2.63 Å, and a corresponding solid angle was found to be 9.46% (Scheme 2). For comparison, an atom in an idealized octahedral environment has six VDP faces with a solid angle of 16.7% for each bond. In a pentanuclear $Cu_5(NIP)_4$ node, the M···M distances vary in a range of 3.20–3.50 Å (Table S5†).[29] There are two unique non-zero contacts in the copper-based node with Ω of 2.60% per contact, giving a total value of 5.20% for the central Cu atom. Despite higher metal node nuclearity observed in $Cu_5(NIP)_4$, estimated Ω for $Cu_5(NIP)_4$ is almost twice as small as that found in $Cu_3(BTC)_2$. Notably, the constructed polyhedra were built taking all atoms in the second and third coordination spheres into account, and only metal nodes are shown in Scheme 2 for clarity. According to the VDP analysis, M···M interactions are not simply a function of metal node nuclearity, and therefore, a more in-depth crystallographic analysis is required for each system. BTC-MOFs could be used as a platform for understanding M–property correlations due to the pronounced M···M interactions.

To evaluate a large number of monometallic and heterometallic systems, we employed XPS as a powerful and non-destructive tool for fast prescreening of the changes in the valence band (VB) region. We simultaneously monitored the DOS near the Fermi level (E_F, binding energy = 0 eV) and changes in the oxidation states of metals integrated into the MOF lattice. Prior to experimental analysis by XPS, all MOF samples were evacuated using the procedures based on the TGA results for the corresponding frameworks (Table 1, Fig. S4, S13–S15, S19, and S20†). The results acquired from XPS studies were compared against those obtained from DR analysis, conductivity measurements, and theoretical modeling. We initially began with $M_{3-X}M'_X(BTC)_2$ due to a wider compositional range and diversity of metals available for integration inside the lattice without degradation of the parent framework.

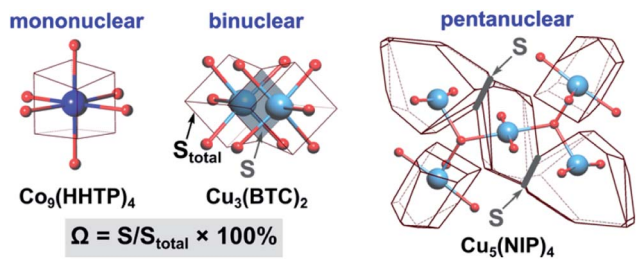

Scheme 2 (Left) VDP of the cobalt atom in the crystal structure of mononuclear $Co_9(HHTP)_4$,[28] (middle) VDP of the copper atoms in the crystal structures of binuclear $Cu_3(BTC)_2$,[31] and (right) pentanuclear $Cu_5(NIP)_4$.[29] The light blue, dark blue, and red spheres represent Cu, Co, and O atoms, respectively. The contact atoms except oxygen for the pentanuclear SBU were omitted for clarity. Gray arrows indicate a shared face of VDP with the area S, while S_{total} stands for the total area of the VDP.

Binuclear heterometallic $M_{3-X}M'_X(BTC)_2$ frameworks

The VB spectra of the evacuated heterometallic $Cu_{3-X}M'_X(BTC)_2$ (M′ = Mn, Fe, Co, Ni, and Zn) MOFs are shown in Fig. 2, S23, and S24.† Based on the data, we have evaluated the onset of the VB as the binding energy at the intersection of a fitted line, representing the average baseline signal, and a fitted tangent line, representing the slope of intensity *vs.* binding energy (Table S6 and Fig. S24; see more information in the ESI†). Fig. 3b demonstrates the dependence of $(E'^* - E')/X_{M'}$ as a function of the second metal (where $\Delta E' = E'^* - E'$; E' and E'^* = VB onsets calculated for $Cu_{3-X}M'_X(BTC)_2$ and $Cu_3(BTC)_2$, respectively; $X_{M'}$ = mole fraction of incorporated M′). As shown in Fig. 3b and Table S7,† the highest value of $(E'^* - E')/X_{M'}$ is found for M′ = Co and the values for M′ = Ni, Mn, Fe, and Zn are 7–27-fold lower (Table S7†). Furthermore, the $(E'^* - E')/X_{M'}$ values for M′ = Ni, Mn, Fe, and Zn are the same within three standard errors, as shown in Fig. S22.† The calculated $(E'^* - E')/X_{M'}$ values could be considered as a descriptor for MOF electronic properties in terms of conductivity since it serves as a measure of DOS near E_F. For M′ = Co, DOS within 0.5 eV of E_F is observed (characteristic of a semiconductor),[34] and therefore, $\Delta E'/X_{M'} = (E'^* - E')/X_{M'}$ (where $E'^* = 1.88$ eV) is a relatively large number after normalization to the mole fraction of integrated M′. In contrast, for M′ = Ni, Mn, Fe, and Zn, the larger energy gap between the valence band onset and E_F (larger E') is more typical of an insulating material and results in smaller values of $\Delta E'/X_{M'}$ as shown in Fig. 3b. We anticipate that the $\Delta E'/X_{M'}$

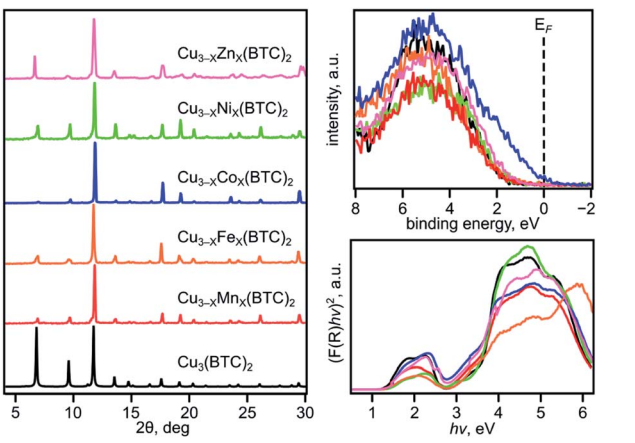

Fig. 2 (Left) PXRD patterns of: $Cu_3(BTC)_2$ (black), $Cu_{2.4}Mn_{0.6}$-BTC (red), $Cu_{2.2}Fe_{0.8}$-BTC (orange), $Cu_{2.8}Co_{0.2}$-BTC (dark blue), $Cu_{2.7}Ni_{0.3}$-BTC (light green), and $Cu_{1.6}Zn_{1.4}$-BTC (pink). (top right) XPS data showing the valence band regions for: $Cu_3(BTC)_2$ and $Cu_{3-X}M'_X(BTC)_2$ (M′ = Mn, Fe, Co, Ni, and Zn) following the same color coding as the PXRD patterns. (bottom right) Tauc plots ($[F(R) \times h\nu]^2$ *vs.* $h\nu$) constructed from DR data for $Cu_3(BTC)_2$ and $Cu_{3-X}M'_X(BTC)_2$ (where M′ = Mn, Fe, Co, Ni, and Zn) following the same color coding as the PXRD patterns.

values describe the electronic properties of the MOFs and should correlate with experimental conductivity and optical properties (Fig. 3a). To test this hypothesis, we initially studied heterometallic samples using DR spectroscopy. The optical band gaps (E_g) of the evacuated BTC-systems were estimated based on the Tauc plot analysis shown in Fig. 2 and S26.† As in the case of $\Delta E'/X_{M'}$ values, the same dependence of $(E_g^* - E_g)/X_{M'}$ from the nature of the metal was observed (E_g^* and E_g = estimated optical band gaps for $Cu_3(BTC)_2$ and $Cu_{3-x}M'_x(BTC)_2$, respectively; $X_{M'}$ = mole fraction of incorporated M′, Fig. 3b). Estimated $\Delta E_g/X_{M'}$ is in line with the tendency observed for $\Delta E'/X_{M'}$, *i.e.*, the largest values for both $\Delta E'/X_{M'}$ and $\Delta E_g/X_{M'}$ correspond to Co/Cu heterometallic samples (Table S9†). As a next step, we evaluated changes in conductivity of these samples. For that, we performed pressed-pellet conductivity measurements using a home-built two-probe device.[35] The list of measured values and a description of sample preparation are presented in Table S10 and the ESI,† respectively. In our studies, we did not focus on each separate measured value (that could be affected by many parameters) but rather tried to establish trends similar to those discussed for optical and VB data (*vide supra*). Indeed, $|(\sigma - \sigma^*)|/X_{M'}$ demonstrated the exact same behavior as that observed for band gap, $\Delta E_g/X_{M'}$, values (Fig. 3b, $|\Delta\sigma| = |\sigma - \sigma^*|$; σ^* and σ = conductivity values for $Cu_3(BTC)_2$ and $Cu_{3-x}M'_x(BTC)_2$, respectively; $X_{M'}$ = mole fraction of incorporated M′). The corresponding graphs with error bars are shown in Fig. S22.† To summarize, all three M′−function correlations, $\Delta E_g/X_{M'}$, $\Delta E'/X_{M'}$, and $|\Delta\sigma|/X_{M'}$ follow the same trend (Fig. 3b) in that the values are highest for Co and generally decrease as Ni, Mn, Fe, and Zn are substituted as M′, respectively. Moreover, $\Delta E_g/X_{M'}$ and $|\Delta\sigma|/X_{M'}$ demonstrate the same dependence for $Cu_{3-x}M'_x(BTC)_2$ where M′ = Ni, Mn, Fe, and Zn. Based on the experimentally acquired data, we can conclude that integration of cobalt as M′ inside $Cu_{3-x}M'_x(BTC)_2$ resulted in a decrease of the optical band gap, appearance of a more pronounced DOS near E_F, and enhancement of conductivity values per cobalt atom, whereas the presence of zinc in the $Cu_{3-x}M'_x(BTC)_2$ lattice led to an increase in band gap and promotion of insulating behavior. Both of these statements are supported by theoretical calculations as described later.

The XPS studies not only allowed us to estimate $(E'^* - E')/X_{M'}$ values, but also shed light on the oxidation states of the incorporated metals (M′). As previously shown for the monometallic $Cu_3(BTC)_2$ system, the $Cu(2p_{3/2})$ region of the XPS spectrum consists of two peaks at 933.0 and 934.7 eV that can be assigned to Cu^{1+} and Cu^{2+}, respectively.[36] For the heterometallic $Cu_{3-x}M'_x(BTC)_2$ MOFs, a similar trend was observed, and the presence of Cu^{1+} and Cu^{2+} peaks was also detected (Fig. S27†). Analysis of the corresponding XPS regions for incorporated M′ allowed us to conclude that M′ inside $Cu_{3-x}M'_x(BTC)_2$ possesses the following oxidation states: +2 (Co); +2 (Ni); +2 (Mn); +2 and +3 (Fe); and +2 (Zn). Based on the XPS data, we attempted to estimate how $(z_{Cu} \times X_{Cu})$ and $(z_{M'} \times X_{M'})$ changes as a function of M′ with the assumption that the total charge of cations remains constant (eqn (2)).

$$z_{M'} \times X_{M'} + z_{Cu} \times X_{Cu} = \text{constant} \quad (2)$$

where $z_{M'}$ and z_{Cu} = charge on M′ and Cu, respectively; $X_{M'}$ and X_{Cu} = mole fraction of M′ and Cu, respectively.

We estimated the average charge on the copper ions by peak fitting the $Cu(2p_{3/2})$ XPS data with contributions from Cu^{1+} and Cu^{2+} (Fig. S27†). For instance, if the ratio of Cu^{1+} to Cu^{2+} is 0.5 to 0.5 then $z_{Cu} = 0.5 \times (1+) + 0.5 \times (2+) = (1.5+)$, where 1+ and 2+ are the charges on copper. The mole fractions of $X_{M'}$ and X_{Cu} were estimated from the ICP-MS data. To find the constant from eqn (2), we used XPS data for monometallic $Cu_3(BTC)_2$. In this case, $(z_{M'} \times X_{M'})$ equals zero because of the absence of a second metal, M′, in the $Cu_3(BTC)_2$ structure. Therefore, $z_{Cu} \times X_{Cu} + z_{M'} \times X_{M'} = z_{Cu} \times (1) + z_{M'} \times (0) = z_{Cu}$. The constant in eqn (2) was estimated to be 1.69. Finally, the $z_{M'}$ value was also calculated based on eqn (2) since z_{Cu} and X_{Cu} (or $X_{M'}$) was estimated from the XPS and ICP-MS data, respectively. The corresponding

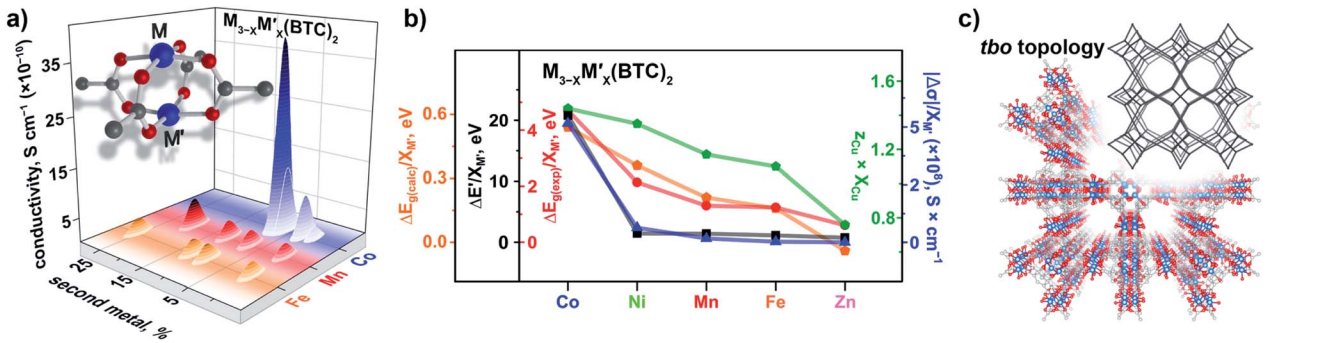

Fig. 3 (a) A binuclear paddle-wheel metal node and graphical illustration of the results of conductivity measurements obtained for $Cu_{3-x}M'_x(BTC)_2$ (M′ = Mn, Fe, and Co) as a function of M′ percentage. (b) Changes in conductivity ($|\Delta\sigma|$, dark blue triangles), experimentally measured band gaps ($\Delta E_{g(exp)}$, red circles), calculated band gaps ($\Delta E_{g(calc)}$, orange pentagons), estimated valence band onset values from the XPS data ($\Delta E'$, black squares), and calculated ($z_{Cu} \times X_{Cu}$) values (green pentagons) as a function of M′ performed for $M_{3-x}M'_x(BTC)_2$ (M′ = Co, Ni, Mn, Fe, and Zn). The ΔE_g, $\Delta E'$, and $|\Delta\sigma|$ values have been normalized to the mole fraction of M′ ($X_{M'}$). The corresponding graphs with error bars are shown in Fig. S22.† (c) Crystal structure of parent $Cu_3(BTC)_2$ possessing the **tbo** topology (shown in inset). The red, gray, and light blue spheres represent O, C, and Cu atoms, respectively. H atoms were omitted for clarity.

Table 2 The $(z_{Cu} \times X_{Cu})$, $(z_{M'} \times X_{M'})$, E', σ, and E_g values estimated for $Cu_{3-x}M'_x(BTC)_2$[a] and $Cu_{3-x}M'_x(HHTP)_2$

M′=	Co	Ni	Mn	Fe	Zn
$Cu_{3-x}M'_x(BTC)_2$					
$z_{Cu} \times X_{Cu}$	1.44	1.35	1.17	1.10	0.89
$z_{M'} \times X_{M'}$	0.25	0.34	0.52	0.59	0.79
E', eV	0.29 ± 0.02	1.72 ± 0.12	1.66 ± 0.17	1.76 ± 0.14	1.50 ± 0.09
σ ($\times 10^{11}$), S × cm^{-1}	396.00 ± 0.19	101.00 ± 0.05	62.40 ± 0.08	36.30 ± 0.03	31.50 ± 0.01
$E_{g(exp)}$, eV	3.22 ± 0.17	3.32 ± 0.13	3.30 ± 0.14	3.24 ± 0.10	3.27 ± 0.09
$E_{g(calc)}$, eV	3.32	3.50	3.65	3.70	3.90
$Cu_{3-x}M'_x(HHTP)_2$					
$z_{Cu} \times X_{Cu}$	1.19	0.77	1.01	—	—
$z_{M'} \times X_{M'}$	0.33	0.75	0.51	—	—
E', eV	1.20 ± 0.07	1.38 ± 0.08	1.11 ± 0.06	—	—
σ ($\times 10^{7}$), S × cm^{-1}	205.00 ± 1.36	0.99 ± 0.01	87.70 ± 0.88	—	—
E_g, eV	1.06 ± 0.01	1.20 ± 0.01	1.17 ± 0.01	—	—

[a] Samples with the maximum M′/Cu ratio were chosen for analysis.

values of $(z_{Cu} \times X_{Cu})/(z_{M'} \times X_{M'})$ for heterometallic BTC-samples with an integrated metal (M′) were found to be 1.44/0.25 (Co), 1.35/0.34 (Ni), 1.17/0.52 (Mn), 1.10/0.59 (Fe), and 0.89/0.79 (Zn, Table 2 and Fig. S27†). The calculated $z_{Cu} \times X_{Cu}$ follows the trends established for the experimental optical band gap and conductivity values (Fig. 3b). Thus, increase in the copper charge and its mole fraction correlates with the corresponding optical band gap decrease.

To rationalize the observed experimental trends, we analyzed the electronic structure computed using the Vienna *ab initio* simulation package (VASP)[37,38] with the plane wave basis set. The total and partial DOS were obtained from the single point calculations at experimental geometries using the hybrid HSE06 method[39] followed by geometry optimization (see the ESI†). The results revealed that substitution of one of the two metal centers in the metal node of the MOF truncated model, $Cu_2(OAc)_4$ (Fig. S34†), resulted in an increase of the band gap in the order Co < Ni < Mn < Fe < Zn (Table 2) that is in agreement with the E_g values estimated from the Tauc plot analysis (Fig. S26†). Calculated $\Delta E_{g(calc)}/X_{M'}$ also follows the experimental trend shown in Fig. 3b. The partial-DOS analysis suggests that the decrease in the band gap is associated with changes in the

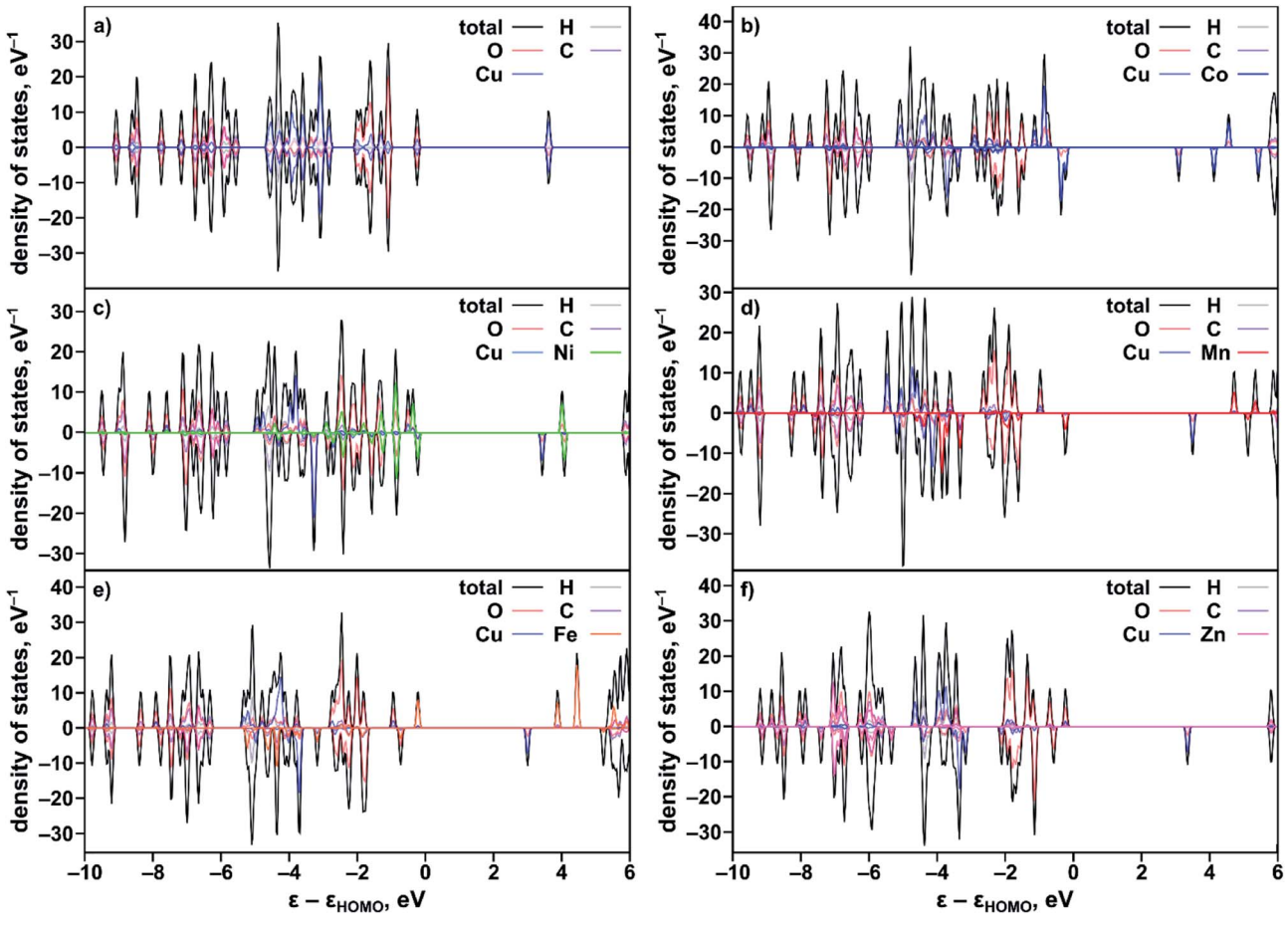

Fig. 4 Partial and total DOS of the studied heterometallic binuclear $M_{3-x}M'_x(BTC)_2$ systems calculated using a truncated cluster model, $Cu_2(OAc)_4$, and the HSE06 exchange-correlation functional: (a) $Cu_2(OAc)_4$, (b) $CuCo(OAc)_4$, (c) $CuNi(OAc)_4$, (d) $CuMn(OAc)_4$, (e) $CuFe(OAc)_4$, and (f) $CuZn(OAc)_4$.

electronic structure near the Fermi level. In the case of M′ = Co, Ni, Mn, and Fe, the highest occupied molecular orbital (HOMO) is dominated by M′-3d-orbitals after substitution, in contrast to parent monometallic $Cu_2(OAc)_4$ where the HOMO is occupied by the O-2p-orbitals (Fig. 4a–e and S35†). At the same time, the lowest unoccupied molecular orbital (LUMO) is dominated by the Cu-3d-orbitals in the case of monometallic and heterometallic clusters. Integration of zinc inside the copper paddle-wheel node, according to theoretical calculations, does not significantly alter the electronic structure, and the band gap edges remain the same (Fig. 4f). The Zn-3d-orbitals lie deep inside the occupied orbitals and the band edges are still dominated by O-2p- and Cu-3d-orbitals that represent the HOMO and LUMO, respectively. These results indicate that cobalt substitution decreases the band gap of Cu-MOF the most, followed by band gaps for Ni < Mn < Fe; while zinc integration has almost no effect on the band gap.

The results of the performed Bader charge, atomic-dipole-corrected-Hishfeld-atomic charge, and Mulliken-charge analysis based on the B3LYP-D3/m6-31G* and ωB97X-V/6-31G* methods using the optimized geometry for the $CuM'(OBn)_4$ (OBn^- = benzoate; M′ = Co, Ni, Mn, Fe, and Zn) cluster are given in Table S13 and described in the ESI.†

As a next step in our analysis, we compared the observed trends for heterometallic MOFs with those known for doped inorganic oxides, which exhibit the electronic property tunability that has been studied for several decades.[40,41] The challenge in the literature search was mainly associated with the typically narrow range of metals traditionally used as dopants for one set of studies. However, we found that Deepak and co-workers reported tuning of electronic properties of ZnO (a wurtzite-type structure) by doping with 3*d* divalent metals such as M′ = Co, Ni, and Mn.[40] It was found that an increase in dopant concentration caused a decrease in the ZnO band gap values ($E_{g(ZnO)}$ = 3.30 eV).[40] Indeed, the reported E_g values of zinc oxide doped with Co, Ni, and Mn were found to be 2.95, 3.24, and 3.28 eV, respectively, for a substitution percentage of M′ at 5% (Fig. 5). Analysis of electronic properties revealed that a decrease in the band gap in the case of the Co dopant is the highest among the three systems, followed by Ni and Mn incorporated samples (Fig. 5). Such a behavior was attributed to the sp–d exchange interactions between electrons in conduction and valence bands (that are mostly s and p electrons) and dopant localized d electrons.[42] In line with this trend, Lin and co-workers reported a theoretical study of the doped anatase phase of TiO_2 with the same transition metals, M′ = Mn, Co, and Ni.[41] *Ab initio* band calculations based on DFT with the plane wave basis set were performed on the supercell of the anatase structure with a substitution percentage of M′ at 12.5%. The trend for Co, Ni, and Mn metals obtained in this study is the following: E_g (1.78 eV for Co : TiO_2) < E_g (2.23 eV for Ni : TiO_2) < E_g (2.32 eV for Mn : TiO_2, Fig. 5). It has been demonstrated that the dopant energy levels occur in the middle of the band gap (at an "intermediate level"), leading to band gap narrowing.[41] While TiO_2 valence and conduction bands are dominated by O-2p and Ti-3d states, respectively, valence and conduction bands are still formed by O-2p and Ti-3d states modified by the dopant metal. On the example of these transition-metal doped oxides, we demonstrate that the trend established for $\Delta E_{g(lit.)}/X_{M'}$ is in line with the trends found in our studies for experimental and calculated $\Delta E_g(Cu_{3-X}M'_X(BTC)_2)/X_{M'}$ (M′ = Co, Ni, and Mn, Fig. 5). Access to crystallographic data of heterometallic MOFs such as $Cu_{3-X}M'_X(BTC)_2$ (M′ = Co, Fe, and Mn, Fig. 3c) allowed us to evaluate the dependence of a unit cell parameter, *a*, ($Cu_{3-X}M'_X(BTC)_2$ belongs to the $Fm\bar{3}m$ space group) as a function of the integrated metal, and therefore survey possible structural distortion. Maximum deviation in the unit cell parameter, *a*, in comparison with that of pristine $Cu_3(BTC)_2$ was found to be 0.09% for $Cu_{1.8}Fe_{1.2}$-BTC while for the rest of the BTC-systems $\Delta a/a^*$ varied in a range of 0.007% to 0.06% (Tables S3 and S4†). Notably, the distance comparison was performed on crystal structures with several M/M′ pairs (M = Cu, M′ = Co; M = Cu, M′ = Fe; and M = Cu, M′ = Mn), collected at the same temperature, 100 K. The evaluation of possible changes in Cu···M′ metal distances demonstrated that the largest change (1.02%) was observed for $Cu_{2.4}Mn_{0.6}$-BTC. The largest change in distances between metal nodes (0.09%) was observed for $Cu_{1.8}Fe_{1.2}$-BTC (Tables S3 and S4†). We also evaluated structural changes by calculating $\Delta a/X_{M'}$ values. Since we have two crystal structures per metal composition, we estimated $\Delta a/X_{M'} = [(a^* - a_1)/X_{M'1} + (a^* - a_2)/X_{M'2}] \times 0.5$ (a_1 and a_2 = unit cell parameters of two heterometallic structures; a^* = the unit cell parameter of the $Cu_3(BTC)_2$ structure; $X_{M'1}$ and $X_{M'2}$ = mole fraction of incorporated M′ in the particular structure; for more details see ESI†). In summary, there are no significant structural deviations to establish a correlation between Cu···M′ metal distances, metal node distances, or unit cell parameters, and the estimated $\Delta a/X_{M'}$ values do not follow the trend based on conductivity, VB edge, and optical data of $Cu_{3-X}M'_X(BTC)_2$ MOFs as shown in Fig. 3.

As a part of our studies, we surveyed the electronic structure changes in heterometallic MM′-MOFs with the same M and M′ but with a different M to M′ ratio (Fig. 3a). The choice of metal ratios was a balance between incorporation of the

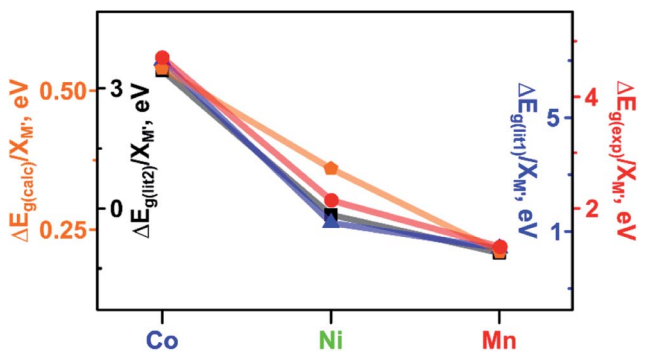

Fig. 5 Band gaps: measured $\Delta E_{g(exp)}$ (red circles) and calculated $\Delta E_{g(calc)}$ (orange pentagons) for $Cu_{3-X}M'_X(BTC)_2$ MOFs. Literature data: measured $\Delta E_{g(lit1)}$ for $M'_{5\%}$:ZnO (dark blue triangles)[40] and calculated $\Delta E_{g(lit2)}$ for $M'_{12.5\%}$:TiO_2 (black squares).[41] ΔE_g values have been normalized to the M′ metal mole fraction (M′ = Co, Ni, and Mn).

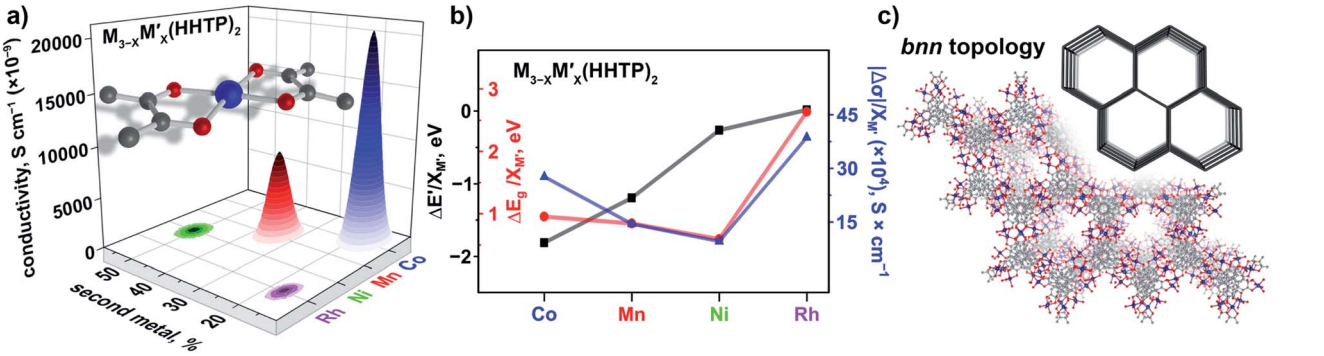

Fig. 6 (a) A mononuclear metal node and graphical illustration of the results of conductivity measurements obtained for $Cu_{3-x}M'_x(HHTP)_2$ as a function of M′ = Co, Mn, Ni, and Rh. (b) Changes in conductivity ($|\Delta\sigma|$, dark blue triangles), experimentally measured band gaps (ΔE_g, red circles), and estimated valence band onset values from the XPS data ($\Delta E'$, black squares) as a function of M′ performed for $Cu_{3-x}M'_x(HHTP)_2$ (M′ = Co, Mn, Ni, and Rh). The ΔE_g, $\Delta E'$, and $|\Delta\sigma|$ values have been normalized to the mole fraction of M′ ($X_{M'}$). The corresponding graphs with error bars are shown in Fig. S37.† (c) Crystal structure of the Co-containing HHTP system possessing the **bnn** topology (shown in inset).[28] The red, gray, and dark blue spheres represent O, C, and Co atoms, respectively. H atoms were omitted for clarity.

highest percentage of the second metal, M′, and preservation of framework integrity. According to conductivity measurements, the largest difference in electronic properties within the same composition was observed for $Cu_{3-x}Co_x(BTC)_2$ systems. Indeed, changes from 2% to 7% of incorporated cobalt according to ICP-MS analysis resulted in a five-fold conductivity enhancement (Fig. 3a and Table S10†). The statistical difference between measured conductivity values was probed by employment of a variance test (ANOVA) integrated in the MATLAB package.[43–45] As a result, it was demonstrated that the conductivity values of the $Cu_{3-x}Co_x(BTC)_2$ samples with different cobalt percentages are indeed statistically different. In the other heterometallic systems with the same M/M′ pairs, the experimentally observed changes as a function of M to M′ ratio were less pronounced in comparison with those observed for $Cu_{3-x}Co_x(BTC)_2$. For instance, changes in iron percentage from 9 to 25% in $Cu_{3-x}Fe_x(BTC)_2$ do not lead to significant changes of electronic properties as shown by conductivity measurements (Fig. 3). Indeed, for $Cu_{3-x}Fe_x(BTC)_2$, the estimated *p*-value was greater than 0.05, and thus, the null hypothesis, that measured conductivity values are the same, could not be rejected. At the same time, the one-way analysis of variance performed for the $Cu_{3-x}Mn_x(BTC)_2$ system demonstrates that the measured conductivity values are statistically different.

Mononuclear heterometallic $M_{3-x}M'_x(HHTP)_2$ frameworks

In contrast to three-dimensional BTC-systems, monometallic $Cu_3(HHTP)_2$ and $Co_9(HHTP)_4$ MOFs are two-dimensional frameworks with a relatively high intrinsic conductivity.[30,46] Since metal nodes are mononuclear in $M_{3-x}M'_x(HHTP)_2$, each M or M′ is separated from one another by an organic linker. However, presence of a second metal, M′ = Co, Ni, Mn, and Rh, in the $Cu_{3-x}M'_x(HHTP)_2$ lattice still affects the material electronic profile. Similar to $Cu_{3-x}M'_x(BTC)_2$, the main changes in the electronic structure of $Cu_{3-x}M'_x(HHTP)_2$ appeared after cobalt incorporation.

However, in contrast to BTC-frameworks, conductivity of heterometallic HHTP-MOFs decreases upon incorporation of a second metal in comparison with that of their monometallic analogues. We estimated the conductivity values as $(2.10 \pm 0.01) \times 10^{-5}$ S × cm^{-1} for $Cu_{2.5}Co_{0.5}$-HHTP, $(8.80 \pm 0.09) \times 10^{-6}$ S cm^{-1} for $Cu_{2.0}Mn_{1.0}$-HHTP, $(9.90 \pm 0.06) \times 10^{-8}$ S cm^{-1} for $Cu_{1.5}Ni_{1.5}$-HHTP, and the lowest value was found to be $(8.60 \pm 0.02) \times 10^{-9}$ S cm^{-1} for the $Cu_{2.6}Rh_{0.4}$-HHTP framework (Tables 2 and S10†); while conductivity measured under the same conditions for the parent $Cu_3(HHTP)_2$ framework was found to be $(4.90 \pm 0.02) \times 10^{-4}$ S × cm^{-1} (Fig. 6a). Previous literature reports for similar 2D frameworks are in line with our studies.[28,47] Thus, it was shown through theoretical modeling that the nickel-to-copper transmetallation procedure in M-HITP systems ($HITP^{3-}$ = 2,3,6,7,10,11-hexaaminotriphenylenesemiquinonate) possessing the same AAAA packing motif can result in changes of the framework electronic behavior from semiconducting to metallic due to different coordination environments adopted by nickel *versus* copper that likely leads to packing distortion.[48] As we previously mentioned, $Cu_3(HHTP)_2$ possesses AAAA packing while layers of $Co_9(HHTP)_4$ alternate in the ABAB sequence.[28] While the A layer in both frameworks consists of the $M_3(HHTP)_2$ two-dimensional honeycomb structure, the B layer in the case of $Co_9(HHTP)_4$ is formed by discrete $Co_3(HHTP)$ units resulting in a $Co_6(HHTP)_2$ layer (Fig. 6c).[28] Therefore, we speculate that changes in electronic behavior of heterometallic HHTP-systems may be indicative of a structural distortion of the 2D sheets due to distinct coordination environments adopted by M and M′. PXRD analysis demonstrated that all $Cu_{3-x}M'_x(HHTP)_2$ possess AAAA stacking that allows for comparison of electronic properties of bimetallic MOFs. To probe possible M′–property correlations similar to the BTC-system, we have evaluated $|\Delta\sigma|/X_{M'}$ as shown in Fig. 6b. Although the unnormalized conductivity values (σ) decrease for Co < Mn < Ni < Rh, the corrected values $|\Delta\sigma|/X_{M'}$ (σ* and σ = conductivity values for $Cu_3(HHTP)_2$ and $Cu_{3-x}M'_x(HHTP)_2$, respectively) do not demonstrate M′–conductivity dependence (Fig. 6b). The optical data (E_g, Table 2) corroborated the trend observed for conductivity values, σ. The smallest band gap among all heterometallic HHTP-systems was detected after integration of Co (1.06 eV) and an

increase in E_g values was observed for M′ = Mn (1.17 eV) < Ni (1.20 eV) < Rh (1.23 eV, Table S8†). However, adjustments based on the mole fraction of integrated metal by estimation of $\Delta E_g/X_{M'}$ (E_g and E_g* = band gap values for $Cu_3(HHTP)_2$ and $Cu_{3-X}M'_X(HHTP)_2$, respectively) did not result in the M′–E_g correlation similar to that observed for $Cu_{3-X}M'_X(BTC)_2$ systems (Fig. 5).

The oxidation states for incorporated M′ = Mn, Ni, and Co inside the HTTP-systems coincide with the values observed for the BTC-systems. Indeed, XPS analysis of the Mn(2p), Ni(2p), and Co(2p) regions of both systems reveals the following oxidation states +2 (Mn), +2 (Ni), and +2 (Co) (see the ESI for more details, Fig. S28–S30†). Furthermore, analysis of the Rh(3d) region indicates the presence of rhodium in the +3 oxidation state (310 eV, Fig. S33†) for the HHTP system. According to XPS studies, the highest DOS near E_F was detected for $Cu_{3-X}Co_X(HHTP)_2$ and $Cu_{3-X}Mn_X(HHTP)_2$ based on the E' values (Tables 2 and S6†). For other HHTP-systems where M′ = Ni (E' = 1.38 eV for $Cu_{3-X}Ni_X(HHTP)_2$, Table S6†) and Rh (E' = 1.51 eV for $Cu_{3-X}Rh_X(HHTP)_2$, Table S6†), the DOS near the Fermi edge are less pronounced (Fig. S40†). Overall, for the $Cu_{3-X}M'_X(HHTP)_2$ system after incorporation of the first–row transition metals, E' values vary in the range of 1.10–1.38 (eV) while for BTC-frameworks E' changes from 1.50 eV (Zn) to 1.76 eV (Fe) with the exception of the Co-incorporated sample (E' = 0.29 eV, Tables 2 and S6†). The larger E' values are consistent with conductivity values, σ (Tables 2 and S10†), which demonstrate that HHTP-frameworks are in general more conductive than the BTC-systems. Similar to BTC-frameworks, we estimated ($z_{M'} \times X_{M'}$ and $z_{Cu} \times X_{Cu}$) changes as a function of M′ in HHTP-systems (where $z_{M'}$ (z_{Cu}) = charge on the metal (copper); $X_{M'}$ (X_{Cu}) = mole fraction of M′ (Cu)). Similar to calculations performed for the BTC-systems (*vide supra*), the constant from eqn (2) was estimated to be 1.53 from the XPS spectrum of the monometallic $Cu_3(HHTP)_2$ sample.

The corresponding values of ($z_{Cu} \times X_{Cu}/z_{M'} \times X_{M'}$) for incorporated Co, Mn, and Ni were found to be 1.19/0.33, 1.01/0.51, and 0.77/0.75, respectively (Table 2 and Fig. S39†).

Pentanuclear heterometallic $M_{5-X}M'_X(NIP)_4$ frameworks

The choice of a $M_5(NIP)_4$ framework for our studies was based on several facts such as, it possesses a larger metal node ensemble size with nuclearity = 5, and therefore, the possibility of stronger metal–metal interactions and electron coupling.[49,50] However, the pentanuclear metal cluster resulted in a significant complication for the second metal with the incorporation. Thus, the main challenge in the case of pentanuclear heterometallic $Cu_{5-X}M'_X(NIP)_4$ systems was preservation of framework integrity after M′ integration. We were able to successfully incorporate Mn, Fe, and Rh inside the $Cu_{5-X}M'_X(NIP)_4$ framework according to the ICP-MS analysis. The oxidation states for incorporated Mn and Rh were found to be +2 and +3, respectively, based on XPS data (Fig. S32 and S33†). Oxidation states of iron were not elucidated due to a low signal-to-noise ratio. However, despite the source of the cobalt (*e.g.*, $Co(NO_3)_2 \cdot 6H_2O$, $CoCl_2 \cdot 6H_2O$, or $Co(OAc)_2 \cdot 4H_2O$) and a number of synthetic conditions, our attempts to integrate Co inside the $Cu_5(NIP)_4$ lattice resulted in amorphous powders that distinguish the NIP-systems from the previously discussed BTC- and HHTP-frameworks. The measured conductivity values are (4.30 ± 0.02) $\times 10^{-6}$ S $\times$ cm^{-1} ($Cu_{4.8}Mn_{0.2}$-NIP), (1.20 ± 0.01) $\times 10^{-7}$ S $\times$ cm^{-1} ($Cu_{4.4}Fe_{0.6}$-NIP), and (1.30 ± 0.04) $\times 10^{-8}$ S $\times$ cm^{-1} ($Cu_{4.8}Rh_{0.2}$-NIP, Fig. 7a). The estimated band gap values from the Tauc plot analysis were found to be 2.91 eV ($Cu_{4.8}Mn_{0.2}$-NIP), 2.76 eV ($Cu_{4.4}Fe_{0.6}$-NIP), and 3.53 eV ($Cu_{4.8}Rh_{0.2}$-NIP). Due to the small number of data points, which is a reflection of synthetic challenges and system complexity (Fig. 7b), we were not able to establish M′–property trends similar to those discussed for BTC-MOFs (Fig. 3). To overcome challenges in structure–property correlations, novel synthetic pathways for access and characterization of heterometallic frameworks with a different composition should be developed first.

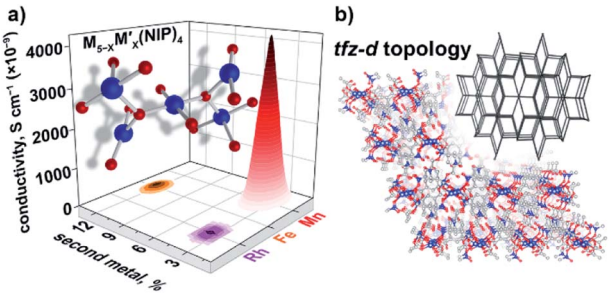

Fig. 7 (a) A pentanuclear metal node and graphical illustration of the results of conductivity measurements obtained for $Cu_{5-X}M'_X(NIP)_4$ as a function of M′ = Rh, Fe, and Mn. (b) Crystal structure of parent $Cu_5(NIP)_4$, possessing the **tfz-d** MOF topology (shown in inset).[29] The red, gray, blue, and dark blue spheres represent O, C, N, and Cu atoms, respectively. H atoms were omitted for clarity.

Conclusions

We probed the electronic profiles of MOFs containing mononuclear, binuclear, and pentanuclear metal nodes as a function of a second metal. For the example of the binuclear BTC-containing heterometallic frameworks, in which the incorporated transition metal (M′) belongs to the first-row, we established a correlation between the changes in the experimentally and theoretically estimated band gaps, ΔE_g, calculated onset values of VB spectra, $\Delta E'$, and conductivity values, $|\Delta\sigma|$. We find that Co-containing MOFs across all $Cu_{3-X}M'_X(BTC)_2$ systems (M′ = Co, Ni, Fe, Mn, and Zn) possess the highest DOS near the Fermi level, which match the theoretically predicted and experimentally estimated band gap values. The origin of the DOS is also discussed according to the theoretical modeling results. In addition, a literature search revealed several similar trends observed previously for oxides doped with 3*d* metals. The results of Bader charge analysis and studies using the Voronoi–Dirichlet partition of crystal structures are also presented. The HHTP-system consisting of mononuclear nodes possesses higher conductivity in comparison with that of the BTC-samples; this behavior correlates with the smaller band gaps observed for HHTP-MOFs in comparison with those of the BTC-frameworks. The NIP-containing frameworks with pentanuclear

metal nodes are the most complex and synthetically challenging among all MOFs studied. Our results for the NIP-frameworks demonstrate the need for both comprehensive analysis of the M′–property tendencies, and novel avenues for preparation of heterometallic multinuclear isoreticular structures. To summarize, the presented studies are the first steps toward understanding and developing the material landscape necessary for on-demand tailoring of electronic properties in heterometallic systems.

Conflicts of interest

There are no conflicts to declare.

Acknowledgements

N. B. S. and D. A. C. are grateful for support from the U.S. Department of Energy, Office of Science and Office of Basic Energy Sciences under Award DE-SC0019360. N. B. S. acknowledges the support from the Sloan Research Fellowship provided by Alfred P. Sloan Foundation and Camille Dreyfus Teaching-Scholar Award provided by Henry and Camille Dreyfus Foundation. S. R. P., S. P., and N. B. S. acknowledge support from the Energy Frontier Research Center funded by the U.S. Department of Energy, Office of Science under Award DE-SC0016574. In addition, we thank the University of South Carolina Advanced Support for Innovative Research Excellence program. S. G. acknowledges partial support from the National Science Foundation EPSCoR Program under NSF Award OIA-1655740/20-GC03.

Notes and references

1 G. Skorupskii and M. Dincă, *J. Am. Chem. Soc.*, 2020, **142**, 6920–6924.
2 J. Li, X. Yu, M. Xu, W. Liu, E. Sandraz, H. Lan, J. Wang and S. M. Cohen, *J. Am. Chem. Soc.*, 2017, **139**, 611–614.
3 D. M. Shakya, O. A. Ejegbavwo, T. Rajeshkumar, S. D. Senanayake, A. J. Brandt, S. Farzandh, N. Acharya, A. M. Ebrahim, A. I. Frenkel, N. Rui, G. L. Tate, J. R. Monnier, K. D. Vogiatzis, N. B. Shustova and D. A. Chen, *Angew. Chem., Int. Ed.*, 2019, **58**, 16533–16537.
4 T. A. Goetjen, X. Zhang, J. Liu, J. T. Hupp and O. K. Farha, *ACS Sustainable Chem. Eng.*, 2019, **7**, 2553–2557.
5 J. Liu, Z. Li, X. Zhang, K.-I. Otake, L. Zhang, A. W. Peters, M. J. Young, N. M. Bedford, S. P. Letourneau, D. J. Mandia, J. W. Elam, O. K. Farha and J. T. Hupp, *ACS Catal.*, 2019, **9**, 3198–3207.
6 Y. Huang, Y. Sun, X. Zheng, T. Aoki, B. Pattengale, J. Huang, X. He, W. Bian, S. Younan, N. Williams, J. Hu, J. Ge, N. Pu, X. Yan, X. Pan, L. Zhang, Y. Wei and J. Gu, *Nat. Commun.*, 2019, **10**, 982.
7 S. Yang, B. Pattengale, S. Lee and J. Huang, *ACS Energy Lett.*, 2018, **3**, 532–539.
8 D. J. Xiao, J. Oktawiec, P. J. Milner and J. R. Long, *J. Am. Chem. Soc.*, 2016, **138**, 14371–14379.
9 W. Liu, W. P. Lustig and J. Li, *EnergyChem*, 2019, **1**, 100008.
10 M. Bornstein, D. M. Parker, A. D. Quast, J. S. Shumaker-Parry and I. Zharov, *ChemCatChem*, 2019, **11**, 4360–4367.
11 A. D. Quast, M. Bornstein, B. J. Greydanus, I. Zharov and J. S. Shumaker-Parry, *ACS Catal.*, 2016, **6**, 4729–4738.
12 M. J. Neufeld, J. L. Harding and M. M. Reynolds, *ACS Appl. Mater. Interfaces*, 2015, **7**, 26742–26750.
13 A. M. Rice, G. A. Leith, O. A. Ejegbavwo, E. A. Dolgopolova and N. B. Shustova, *ACS Energy Lett.*, 2019, **4**, 1938–1946.
14 L. Sun, C. H. Hendon, S. S. Park, Y. Tulchinsky, R. Wan, F. Wang, A. Walsh and M. Dincă, *Chem. Sci.*, 2017, **8**, 4450–4457.
15 L. Sun, C. H. Hendon, S. S. Park, Y. Tulchinsky, R. Wan, F. Wang, A. Walsh and M. Dincă, *Chem. Sci.*, 2017, **8**, 4450–4457.
16 K. C. Bentz and S. M. Cohen, *Angew. Chem., Int. Ed.*, 2018, **57**, 14992–15001.
17 Z. Chen, S. L. Hanna, L. R. Redfern, D. Alezi, T. Islamoglu and O. K. Farha, *Coord. Chem. Rev.*, 2019, **386**, 32–49.
18 X. Zhao, M. S. Shimazu, X. Chen, X. Bu and P. Feng, *Angew. Chem., Int. Ed.*, 2018, **57**, 6208–6211.
19 Y. Liao, L. Zhang, M. H. Weston, W. Morris, J. T. Hupp and O. K. Farha, *Chem. Commun.*, 2017, **53**, 9376–9379.
20 H. Wang, X. Dong, J. Lin, S. J. Teat, S. Jensen, J. Cure, E. V. Alexandrov, Q. Xia, K. Tan, Q. Wang, D. H. Olson, D. M. Proserpio, Y. J. Chabal, T. Thonhauser, J. Sun, Y. Han and J. Li, *Nat. Commun.*, 2018, **9**, 1745.
21 N. R. Catarineu, A. Schoedel, P. Urban, M. B. Morla, C. A. Trickett and O. M. Yaghi, *J. Am. Chem. Soc.*, 2016, **138**, 10826–10829.
22 M. J. Kalmutzki, N. Hanikel and O. M. Yaghi, *Sci. Adv.*, 2018, **4**, eaat9180.
23 L. S. Xie, L. Sun, R. Wan, S. S. Park, J. A. DeGayner, C. H. Hendon and M. Dincă, *J. Am. Chem. Soc.*, 2018, **140**, 7411–7414.
24 Q. G. Zhai, X. Bu, C. Mao, X. Zhao and P. Feng, *J. Am. Chem. Soc.*, 2016, **138**, 2524–2527.
25 J. G. Park, M. L. Aubrey, J. Oktawiec, K. Chakarawet, L. E. Darago, F. Grandjean, G. J. Long and J. R. Long, *J. Am. Chem. Soc.*, 2018, **140**, 8526–8534.
26 S. Yuan, J.-S. Qin, H.-Q. Xu, J. Su, D. Rossi, Y. Chen, L. Zhang, C. Lollar, Q. Wang, H.-L. Jiang, D. H. Son, H. Xu, Z. Huang, X. Zou and H.-C. Zhou, *ACS Cent. Sci.*, 2018, **4**, 105–111.
27 S. Yuan, J.-S. Qin, J. Su, B. Li, J. Li, W. Chen, H. F. Drake, P. Zhang, D. Yuan, J. Zuo and H.-C. Zhou, *Angew. Chem., Int. Ed.*, 2018, **57**, 12578–12583.
28 M. Hmadeh, Z. Lu, Z. Liu, F. Gándara, H. Furukawa, S. Wan, V. Augustyn, R. Chang, L. Liao, F. Zhou, E. Perre, V. Ozolins, K. Suenaga, X. Duan, B. Dunn, Y. Yamamto, O. Terasaki and O. M. Yaghi, *Chem. Mater.*, 2012, **24**, 3511–3513.
29 Y. Zhao, M. Padmanabhan, Q. Gong, N. Tsumori, Q. Xu and J. Li, *Chem. Commun.*, 2011, **47**, 6377–6379.
30 M. Ko, A. Aykanat, M. K. Smith and K. A. Mirica, *Sensors*, 2017, **17**, 2192.
31 S. S.-Y. Chui, S. M.-F. Lo, J. P. H. Charmant, A. G. Orpen and I. D. Williams, *Science*, 1999, **283**, 1148–1150.
32 V. A. Blatov and V. N. Serezhkin, *Russ. J. Inorg. Chem.*, 2000, **45**, S105−S222.

33 V. A. Blatov, A. P. Shevchenko and D. M. Proserpio, *Cryst. Growth Des.*, 2014, **14**, 3576–3586.
34 E. A. Dolgopolova, A. J. Brandt, O. A. Ejegbavwo, A. S. Duke, T. D. Maddumapatabandi, R. P. Galhenage, B. W. Larson, O. G. Reid, S. C. Ammal, A. Heyden, M. Chandrashekhar, V. Stavila, D. A. Chen and N. B. Shustova, *J. Am. Chem. Soc.*, 2017, **139**, 5201–5209.
35 O. A. Ejegbavwo, C. R. Martin, O. A. Olorunfemi, G. A. Leith, R. T. Ly, A. M. Rice, E. A. Dolgopolova, M. D. Smith, S. G. Karakalos, N. Birkner, B. A. Powell, S. Pandey, R. J. Koch, S. T. Misture, H.-C. zur Loye, S. R. Phillpot, K. S. Brinkman and N. B. Shustova, *J. Am. Chem. Soc.*, 2019, **141**, 11628–11640.
36 A. S. Duke, E. A. Dolgopolova, R. P. Galhenage, S. C. Ammal, A. Heyden, M. D. Smith, D. A. Chen and N. B. Shustova, *J. Phys. Chem. C*, 2015, **119**, 27457–27466.
37 G. Kresse and J. Hafner, *Phys. Rev. B: Condens. Matter Mater. Phys.*, 1993, **47**, 558–561.
38 G. Kresse and J. Furthmüller, *Phys. Rev. B: Condens. Matter Mater. Phys.*, 1996, **54**, 11169–11186.
39 A. D. Becke, *J. Chem. Phys.*, 1993, **98**, 5648–5652.
40 S. V. Bhat and F. L. Deepak, *Solid State Commun.*, 2005, **135**, 345–347.
41 Y. Wang, R. Zhang, J. Li, L. Li and S. Lin, *Nanoscale Res. Lett.*, 2014, **9**, 46.
42 K. J. Kim and Y. R. Park, *Appl. Phys. Lett.*, 2002, **81**, 1420–1422.
43 H.-S. Oh, *Biometrics*, 2013, **69**, 1086–1089.
44 D. B. Rorabacher, *Anal. Chem.*, 1991, **63**, 139–146.
45 R. F. Hirsch, *Anal. Chem.*, 1977, **49**, 691A–700A.
46 L. Mendecki and K. A. Mirica, *ACS Appl. Mater. Interfaces*, 2018, **10**, 19248–19257.
47 M. K. Smith and K. A. Mirica, *J. Am. Chem. Soc.*, 2017, **139**, 16759–16767.
48 S. Chen, J. Dai and X. C. Zeng, *Phys. Chem. Chem. Phys.*, 2015, **17**, 5954–5958.
49 F. Karsai, M. Engel, E. Flage-Larsen and G. Kresse, *New J. Phys.*, 2018, **20**, 123008.
50 M. Muthukrishnaveni and N. Srinivasan, *Phase Transitions*, 2015, **88**, 1174–1180.